Universiteit Utrecht

Department of Physics

X(3872) analysis for run 5 with the O^2 framework

Master Thesis

Rik Spijkers

Supervisor:

Dr. Panos Christakoglou
Institute for Gravitational and Subatomic Physics, Utrecht

Second examiner:

Dr. Alessandro Grelli
Institute for Gravitational and Subatomic Physics, Utrecht

July 9, 2021

Abstract

In this thesis we perform simulation studies on the exotic X(3872) hadron for the future heavy ion detector at the LHC for run 5. The X(3872) is reconstructed via its decay X(3872) $\rightarrow J/\psi\ \pi^+\pi^-$, where $J/\psi \rightarrow e^+e^-$. This is a daunting endeavor in part due to the very low transverse momentum of the pion daughters, but with the proposed upgrades to the detector for run 5 (ALICE 3) this analysis may prove feasible. We provide a framework for the X(3872) reconstruction within the heavy flavour software framework, taking advantage of its modular structure. With a preliminary selection strategy, we report an efficiency ranging from approximately 0.03 to 0.22 for $0< p_{\mathrm{T}} < 15$ GeV/c, with a significance on the order of 10^{-1}. A first look at a different selection strategy provides significant improvements with an efficiency between roughly 0.19 to 0.6, and doubling the significance. This highlights the potential of the analysis on X(3872) for run 5.

Contents

Chapter 1

Introduction

The Standard Model (SM) of particle physics has been extremely successful in describing the fundamental interactions (forces) of nature, with the exception of gravity. It aims to describe physical phenomena with the help of fundamental interactions between elementary particles. The theory behind the Standard Model is known as quantum field theory (QFT), which views the fundamental interactions as quantum fields and elementary particles as excitations of those fields. In particle physics, the fundamental forces within the SM (electromagnetic, weak, strong) are understood as being "mediated" by elementary particles themselves, called bosons. Elementary particles on which these forces act - or in other words, elementary particles that partake in but not mediate these interactions - are called fermions. An overview of the elementary particles in the SM is given in Figure 1.1.

This thesis will predominantly discuss physics within the framework of the strong interaction, described by quantum chromodynamics (QCD). The force acts on so called colour charges (hence *chromo*dynamics), denoted by red, green, blue and their anti-colours. A combination of a colour and its anti-colour is considered neutral, as well as the combination of all three (anti)-colours. Quarks and gluons are the only particles that have a colour charge, and as such are the only participants in the strong interaction with gluons being the mediators. Quarks may form composite particles called hadrons, where mesons consist of a quark and an anti-quark (not necessarily the same quark) and baryons consist of either three quarks or three anti-quarks. Note that these combinations correspond to the neutral colour combinations.

The strong interaction has a few unique characteristics, usually described by the terms "asymptotic freedom" and "colour confinement". The former concerns the behaviour of the strength of the interaction as a function of momentum transfer: the strong coupling constant is a bit of a misnomer, as it is not a constant but depends on the momentum transfer. It increases asymptotically with decreasing momentum transfer, leading to a coupling constant that is so large that perturbative calculations break down. Colour confinement on the other hand, is still a mystery and might be related to how the strength

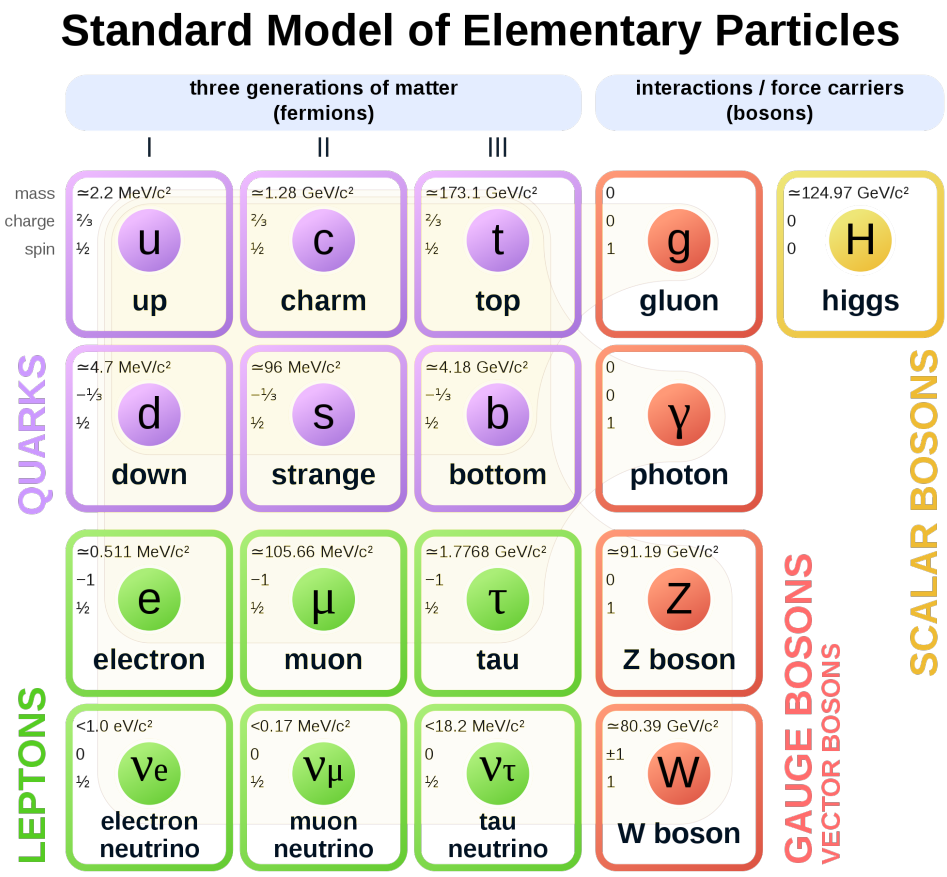

Figure 1.1: The Standard Model of particle physics. Figure taken from [1].

of the strong force changes with distance between two colour charges. While the strength of other forces decreases with distance (gravity and the electromagnetic force famously according to the inverse square law), the strong force actually increases with distance. Consequently, individual quarks and gluons cannot be observed freely in nature.[1]

Colour confinement makes it exceptionally challenging to study the strong interaction. After all, it is difficult to study elementary particles that are not observed freely in nature. The hadrons made up of these quarks and gluons can be thought of as bags containing the quarks and gluons In extremely hot and dense circumstances the boundaries of these bags may start to overlap, and even "disappear", creating a medium known as a quark-gluon plasma (QGP). In this medium quarks may move freely - in other words, they are deconfined. This medium therefore provides a unique insight to the strong interaction. It

[1]One may think of colour confinement as nature choosing the energetically favourable option. At a certain distance, the potential energy of the strong force becomes so great that it is actually favourable to create new colour-charged particles that neutralize the strong force.

should of course be noted that the QGP in and of itself is a very interesting phenomenon, closely related to the origin of the universe. One way of creating such a hot and dense medium is by colliding particles containing many hadrons, such as lead ions, at very high energies. The very energetically dense state right after the collision of these ions allow for the formation of the quark-gluon plasma. The QGP exhibits properties such as hydrodynamical expansion and bulk flow, which affect particles produced early on in the collision.

1.1 Exotic hadron states - the case of X(3872)

According to the quark model we may have combinations of 2 and 3 quarks, i.e. mesons and baryons. However, the underlying theory of QCD allows for more exotic states that were not described initially by the quark model. These states have long been hypothesized to exist by theory and are known, according to their quark content, as tetra- and pentaquarks. The nature of such particles is still largely up for discussion, making them very interesting research avenues. One such particle and the topic of this thesis is the X(3872), first observed in 2003 by the Belle experiment [2]. It consists of a $c\bar{c}$ pair and two light quarks. There are two leading hypotheses concerning the underlaying structure of the X(3872): a tetraquark or a $D^0 - \bar{D}^{*0}$ molecule. The tetraquark is expected to be much more compact compared to a molecular state, where the two mesons are bound by the weak interaction. The two mesons containing a c-quark in the molecular state may be further separated than the c-quarks in a tetraquark state. This could have implications on the production of the X(3872) since the tetraquark state requires two charm quarks to be closer, while the molecular state prefers to have some separation between the charm quarks [3].

This is especially interesting in the context of heavy ion collisions, where the charm quarks are carried by bulk flow of the QGP and are thus expected to be somewhat separated in space. Consequentially, one would expect a larger X(3872) yield in case of the molecular hypothesis compared to the tetraquark. Zhang *et al.* have calculated this effect for the two hypotheses, adopting a multiphase transport model (AMPT), see Figure 1.2a. Not only would one expect a larger effect of the bulk flow in the case of central collisions, the amount of available charm quarks is also higher. In the case of the tetraquark hypothesis, these two effects compete instead of adding onto each other, leading to a relatively flat centrality dependence. [3]

Related to this, Esposito *et al.* [4] have studied differences in X(3872) yield compared to the $\psi(2S)$, another hadron containing two charm quarks, for the two different hypotheses. They implemented the comover interaction model to include interactions of the X(3872) and $\psi(2S)$ with comoving particles in proton-proton collisions. These interactions may effectively break these particles up, large particles being more susceptible to these interactions. This leads to the sharply declining blue line in Figure 1.2b. They have

also extended their model to incorporate coalescence, a hadron production mechanism, leading to a model that clearly contradicts the data. The effect of coalescence is negligible in very compact states, such as the tetraquark. As a consequence of all this, their analysis seems to strongly favour the tetraquark hypothesis. [4]

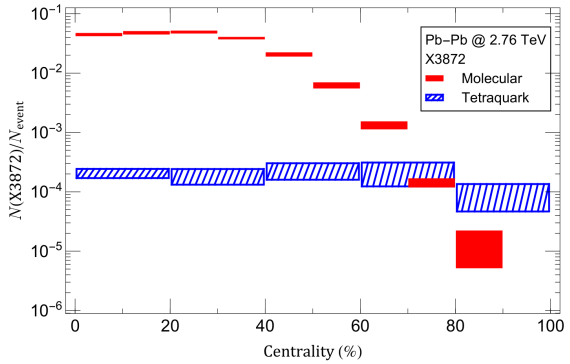

(a) X(3872) yield as a function of centrality for the two different hypotheses. Figure taken from [3].

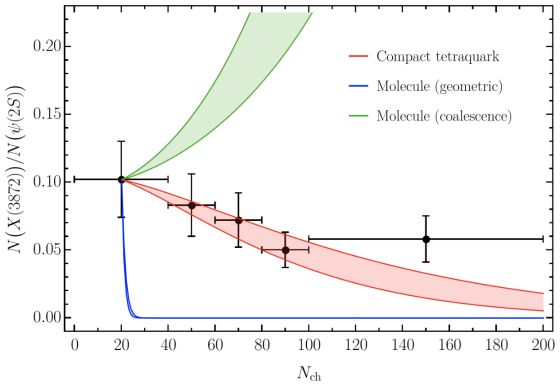

(b) Ratio of X(3872) to $\psi(2S)$ as a function of multiplicity, taken from [4]. The datapoints are from LHCb [5].

Figure 1.2: X(3872) yield.

In this thesis we will present the first analysis of X(3872) $\rightarrow J/\psi\ \pi^+\pi^-$ with $J/\psi \rightarrow e^+e^-$ for run 5 with the O^2 framework. We will first discuss both the current experimental setup and (proposed) upgraded detectors, motivating the X(3872) analysis for run 5. Following this we will describe the software framework used for this analysis, and the strategy implemented for the selection of X(3872) candidates. We present the results of this analysis, most notably the efficiency and significance, before discussing an improved selection strategy. We conclude by discussing the prospects for this analysis.

Chapter 2

The Detector

2.1 CERN and the Large Hadron Collider

In order to shed light on some of the fundamental unanswered questions in physics, physicists need to probe the way particles interact at the smallest scale. This is done by accelerating and colliding particles at high energies. A beam of particles is usually accelerated to high speeds (and therefore high energies) before colliding them with either a fixed target, or another beam of particles. There is an entire accelerator complex built at CERN to achieve this, see Figure 2.1. Starting with the Synchro-Cyclotron (SC) in 1957, CERN's first accelerator, continuous efforts have been made to increase the energy to which the beams can be accelerated. This effort culminated in the construction and operation of a hadron accelerator between 1998 and 2008: the Large Hadron Collider (LHC). The LHC is built inside a circular underground tunnel with a circumference of 26.7 km. Two beams of particles travel in opposite directions, accelerated and steered by thousands of magnets. The beams collide at four different Interaction Points (IP) corresponding with the four major LHC experiments: ALICE, ATLAS, CMS, and LHCb. The LHC started its first run of data taking in 2009. Since then it has completed 2 runs of data taking: run 1 from 2009 to 2013, and run 2 from 2015 to 2018. Although the LHC is theoretically capable of colliding protons at energies of 14 TeV, the first time it will reach this energy is planned to be in run 3, i.e. in the upcoming run planned to start in 2022. The data in run 1 was taken with collision energies of up to 7 TeV, while the run 2 data was taken with energies of up to 13 TeV.

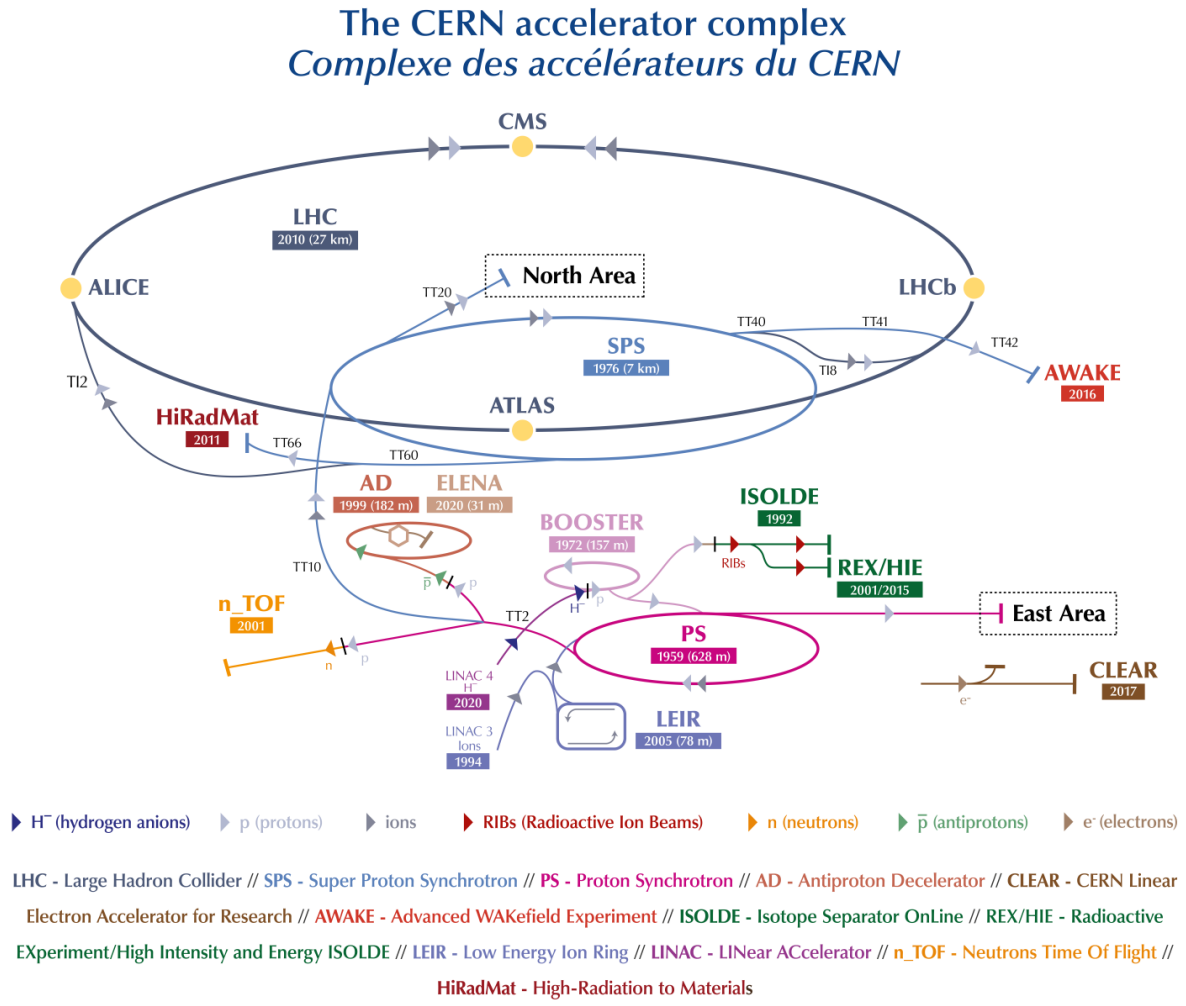

Figure 2.1: The CERN accelerator complex. Figure taken from [6].

2.2 A Large Ion Collider Experiment

Although the main focus of the LHC is on proton-proton (pp) collisions, for usually one month per year the LHC delivers heavy-ion collisions using a Pb source. Besides Pb-Pb collisions, they also produce proton-lead (p-Pb) collisions as an intermediate step between pp and Pb-Pb collisions. One of the main goals of this programme is to study the nature of the quark-gluon plasma. The lead isotope that is used by the LHC has 208 nucleons (82 protons and 126 neutrons), so it is not hard to imagine that p-Pb and Pb-Pb collisions will produce a lot more particles than regular pp collisions. In order to deal with this, a

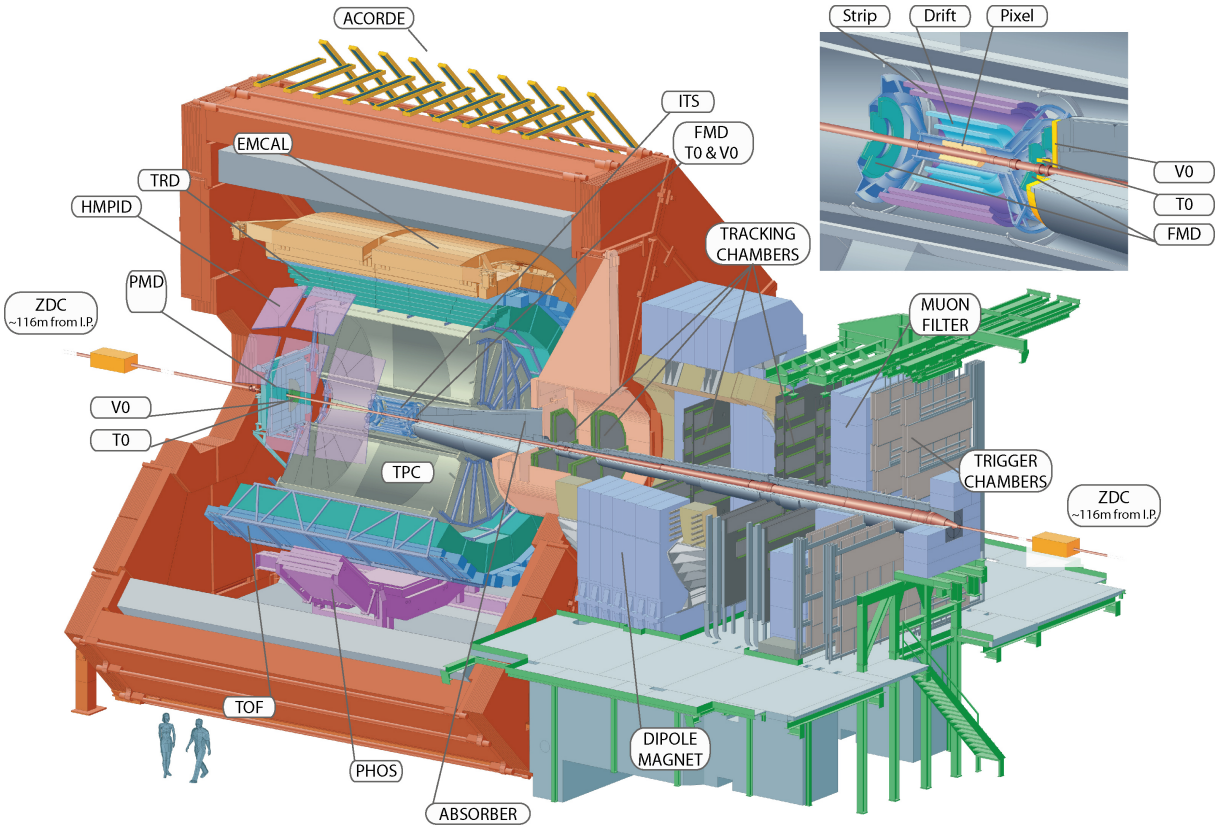

Figure 2.2: A schematic overview of the ALICE detector. Figure taken from [7].

dedicated detector optimized for heavy ion collisions was devised: A Large Ion Collider Experiment (ALICE).

The ALICE detector used in run 1 and run 2 consists of detector systems that can be split into three categories: the central barrel, forward detectors, in addition to a muon spectrometer. The central barrel detectors include (enumerated in order of closest to the beam) the Inner Tracking System (ITS), Time Projection Chamber (TPC), Transition Radiation Detector (TRD), Time Of Flight (TOF), Photon Spectrometer (PHOS), Electromagnetic Calorimeter (EMCal), and High Momentum Particle Identification Detector (HMPID). A schematic cross section of the inner barrel can be seen in Figure 2.3. The central barrel detectors are mainly responsible for the tracking and identification of particles via different physical processes such as ionization energy loss $\mathrm{d}E\,/\,\mathrm{d}x$. [8]

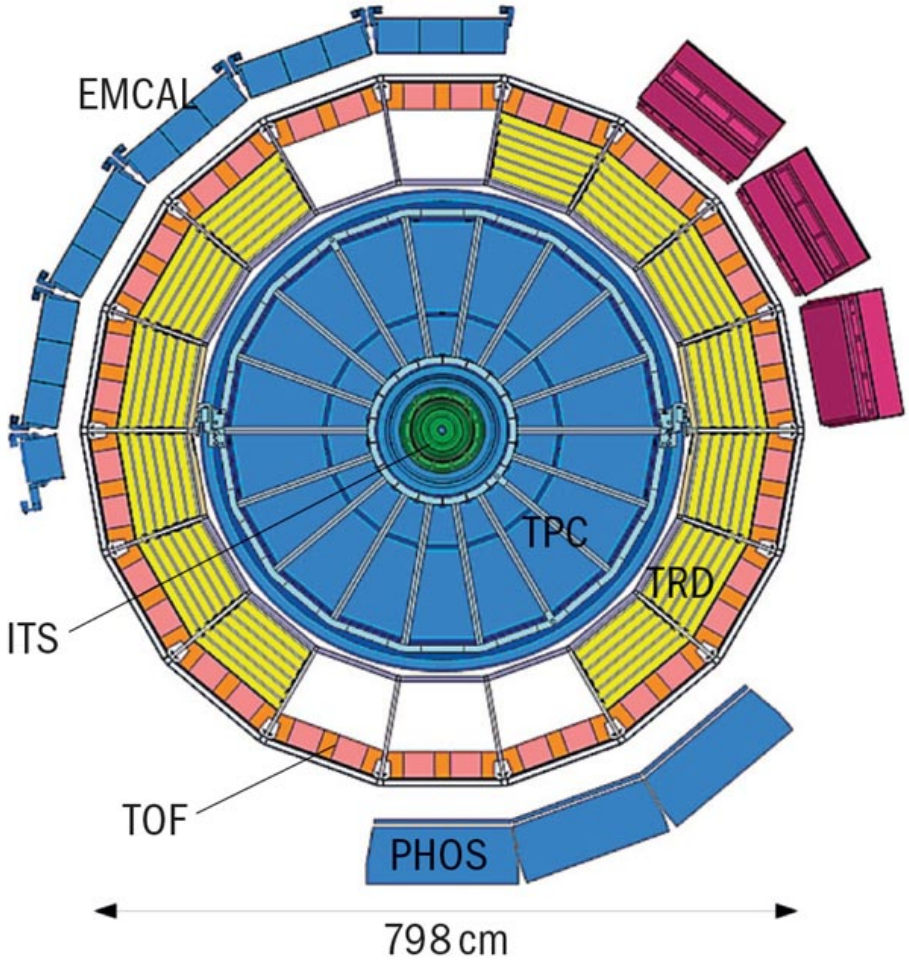

Figure 2.3: A cross section of the ALICE detector in the xy-plane as used in run 1. The three purple blocks in the upper right of the figure represent the HMPID

The forward detectors, among which are the Photon Multiplicity Detector (PMD), Forward Multiplicity Detector (FMD), V0, T0, and Zero Degree Calorimeter (ZDC), are used for a variety of things. The PMD and FMD are used for photon and charged particle detection at higher pseudorapidity regions, usually outside of the central barrel detector range. The T0 is a Cherenkov detector used to determine the time and longitudinal position of the interaction. The V0 is mainly used for triggering purposes and the determination of the centrality in Pb-Pb collisions. The ZDC detects the energy of the spectator nucleons, the nucleons that do not participate in a collision and thus escape from the interaction region, to determine among other things the centrality of Pb-Pb collisions. [8]

The muon spectrometer is, as the name suggests, used to detect muons originating from quarkonium decays. Because quarkonium states consist of a quark-antiquark pair of the same flavour, they are flavour neutral. This allows them to decay via electroweak processes to a pair of leptons such as muons. Because this is a purely leptonic channel it does not suffer from the drawbacks of a very large hadronic background, making it a very appealing way to measure quarkonium. The muon spectrometer consists of Muon Chambers (MCH) and Muon Triggers (MTR), which do exactly what their names suggests. It also uses a hadron absorber to prevent everything except muons from entering the detector. [8]

2.3 High luminosity upgrade

The ALICE collaboration as well as the other experiments, were very successful over the past decade of data acquiring and analyzing at the LHC. Arguably the highlight was the discovery of the long predicted Higgs boson by ATLAS and CMS in 2012, something the LEP was not able to do.[1] The Higgs boson, with a mass of roughly 125 GeV, is considered a heavy particle. Together with hypothetical supersymmetric particles, which were also expected to be heavy, this formed a large part of the motivation for a particle accelerator able to reach high energies in order to give the best shot at deciphering the existence and/or nature of these particles. The results speak for themselves.

Historically speaking, higher energies needed to discover heavier particles have been a recurring theme in experimental particle physics. However, the plans for run 3 and beyond are not motivated by an increase in collision energy, but rather an increase in luminosity: the number of collisions per area per second. In other words, the LHC will focus on drastically increasing the statistics of the samples available for data analysis. This will increase the odds of seeing extremely rare processes and provide the statistics necessary to extract significant results for measurements that suffer from lack of statistics.

One of the frontiers that will benefit a lot from such an increase in statistics is the research on heavy flavour particles: hadrons that contain a charm or a beauty (bottom) quark. These particles are relatively rare because it takes a significant amount of energy to create a particle with a high mass. Some examples in the meson section are the D- and B-mesons, which contain a charm or a beauty quark respectively usually paired with a light quark (up, down, strange). There are also so called charmonium and bottomonium states, which are bound states of a heavy quark with its antiquark. The different states of charmonium and bottomonium are distinguished by their mass or by quantum numbers such as parity and isospin. Examples are the J/ψ (charmonium) and the Υ (bottomonium) mesons. As for the baryon section, typical particles are the $\Lambda_{c,b}$ particles, consisting of a heavy quark paired with an up and a down quark. There are also mesons and baryons

[1] With data from the LEP there were "tantalizing" hints of the Higgs boson at the end of the scheduled run time. However, after extending the run-time for a few months the signal did not increase in significance and the LEP had to make way for the LHC

with multiple heavy quarks such as the B_C meson or the Ξ_{CC}^+ baryon, these are rarer still compared to particles that contain a single heavy quark.

These heavy flavour particles provide a unique opportunity to probe the characteristics of the QGP. Charm and beauty quarks are produced very early in the collision via hard scattering processes, before the QGP forms. This means they experience the entire evolution of the QGP. Adding onto this, their high mass makes it very unlikely they completely thermalize, which means that there is a high chance of preserving information of the interaction. Another advantage of their high mass is that perturbative QCD (pQCD) can be used to make theoretical predictions, since the mass of a heavy quark (a few GeV) is significantly larger than the QCD scale (a few hundred MeV). This all combined makes heavy flavour particles excellent probes. [9]

Measurements of heavy flavour particles require not only high statistics, but also high precision. This is due to the fact that these particles, especially charmed hadrons[2], have very short lifetimes and thus decay very close to the primary-interaction vertex. A high vertex resolution is needed to distinguish this secondary from the primary vertex, in order to determine whether the decay products originate from a heavy flavour decay or from the primary interaction. The ALICE detector will achieve this higher resolution for heavy flavour particles while maintaining its particle identification performance by upgrading the inner barrel detectors, especially the ITS. These upgrades will focus on increasing the proximity of the ITS layers to the beam pipe and decreasing the material budget. In addition to this, all systems will see an increased readout rate to comply with the high interaction rate of the LHC. [9]

Though the ALICE upgrades for run 3 and run 4 are very promising, there are limitations to what such an apparatus can achieve. Simulation studies on the elliptic flow of heavy flavour particles, characterized by the v_2 coefficient [11], for run 3 and run 4 show that there is room for improvement still, see Figure 2.4. While the projections for the D-mesons are quite accurate, the relative uncertainty for the Λ_C^+ are on the order of tens of percents. This makes it impossible to compare theoretical flow models that differ by smaller margins, e.g. a few percent. The Λ_C^+ is a particularly difficult particle to reconstruct due to its short mean proper decay length: 60μm, compared to the $120 - 300\mu$m of the D mesons [9]. For the low transverse momentum region there are no projected results at all, indicating that even with the upgraded detector for run 3 and 4 the low momentum region is challenging.

[2]Charm quarks are kinematically allowed to decay to a quark of the same generation (strange quark), as opposed to beauty quarks. Since the coupling between quarks of the same generation are stronger than couplings spanning one or more generations, this leads to a larger cross section for charm decays and thus a shorter lifetime compared to beauty decays.

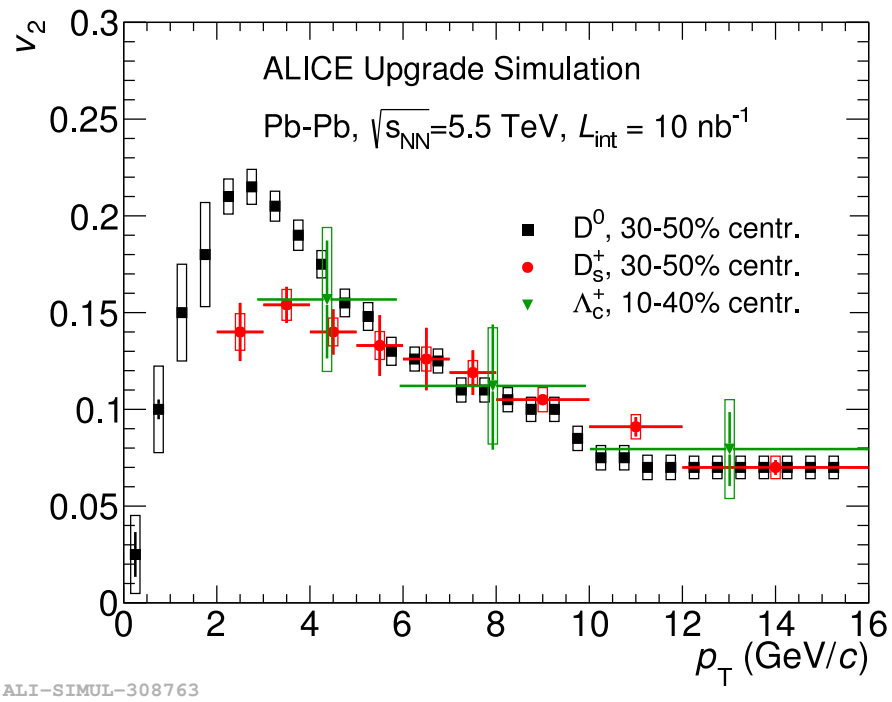

Figure 2.4: Flow coefficient v_2 of charmed hadrons for run 3 and run 4. Figure taken from [10].

2.4 ALICE 3

To reach the precision and low p_{T} region needed for studies on for instance the Λ_C^+, a new detector concept was introduced: ALICE 3. This detector could be installed during the 4th Long Shutdown period (LS4), such that it is operational during run 5. This new detector would apply Complementary Metal-Oxide-Silicon (CMOS) Monolithic Active Pixel Sensors (MAPS) technology to an ultra-low-mass silicon tracker. The fact that these layers of Si-sensors are very thin combined with the proximity to the beam pipe would allow for measurements of particles with p_{T} down to a few tens of MeV/c. In addition to this, the detector layout (see Figure 2.5) of a barrel plus two endcaps would make it possible to cover a large pseudorapidity region: $|\eta| < 4$. This will significantly increase the yield of soft particles. [12]

Not only will the ALICE 3 detector provide higher precision and access to the lower momentum region, the MAPS technology will enable it to run at significantly higher luminosities than the upgraded ALICE experiment: 20 to 50 times higher [12]. This dramatic increase is partially due to the absence of a TPC detector in ALICE 3, which is one of the limiting factors regarding read-out rate. To give an indication of what

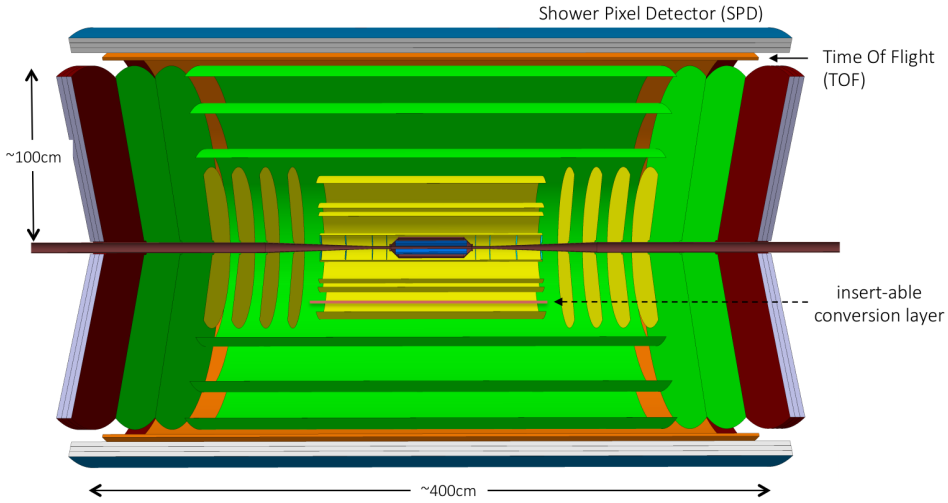

Figure 2.5: Schematic of the ALICE 3 detector. Figure taken from [12].

this increase in luminosity will mean for heavy flavour measurements, projections have been made by scaling the uncertainties by the square root of the number of events while assuming the performance of the upgraded ALICE detector (dedicated studies are needed to analyze the performance of ALICE 3; this is also heavily dependent on the detailed specifications).

The ALICE 3 projections for the Λ_C^+ results shown in Section 2.3 (Figure 2.4) can be seen in Figure 2.6. Without taking into account the upgraded detector, it is already apparent that the relative uncertainty is projected to improve significantly. Adding onto this the ability to improve precision and reach the low p_{T} region, we may expect the relative uncertainty to be on the order of $\sim 1\%$. This would allow for much more accurate analysis on the elliptic flow of the Λ_C^+, as well as meaningful comparisons with theoretical predictions.

2.4.1 X(3872)

Another research avenue that could be in reach with ALICE 3 is the X(3872) analysis; more specifically the X(3872) $\rightarrow J/\psi\ \pi^+\pi^-$ decay channel, with $J/\psi \rightarrow e^+e^-$ or $J/\psi \rightarrow \mu^+\mu^-$. There are multiple aspects of this analysis that make it very challenging. The fact that this is a cascading decay means that we need a lot of statistics for this analysis. This is due to the relatively small branching ratios: a few percent in both the X(3872) $\rightarrow J/\psi\ \pi^+\pi^-$ and the $J/\psi \rightarrow e^+e^-/\mu^+\mu^-$ decays. This means that on the order of $\sim 0.1\%$ of all X(3872)'s decay into the observed channel (double if we reconstruct both the electronic and the muonic decay of the J/ψ). The kinematics of the X(3872) $\rightarrow J/\psi\ \pi^+\pi^-$ also provide a challenge: the mass of the X(3872) is quite close to the mass of the J/ψ

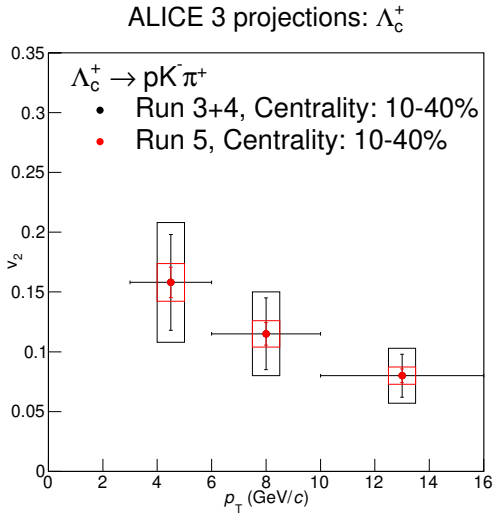

(a) Elliptic flow coefficient v_2 of the Λ_C^+, projected for ALICE 3.

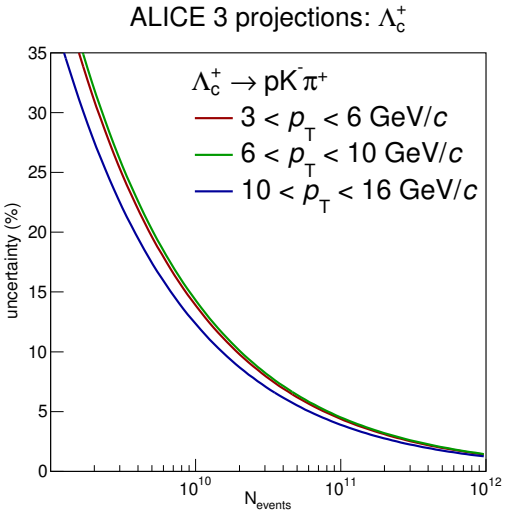

(b) Relative uncertainty of the projections show in (a), as a function of the number of events.

Figure 2.6: Λ_C^+ projections for ALICE 3.

(3097 MeV/c^2), while the J/ψ will also inherit most of the momentum of the X(3872). Consequently, the pions originating from the X(3872) decay are very soft.

As discussed extensively in this section, ALICE 3 will allow for much higher luminosity (and therefore statistics) while also enabling access to the low p_T region. These aspects will both be extremely important in order to measure the X(3872).

Chapter 3

Methods

3.1 The O^2 framework

The drastically increasing interaction rate of the upgraded LHC means that the size of the raw data output will also be increased by roughly two orders of magnitude. Adding onto this that triggering techniques are very inefficient when the signal over background ratio is very small, the data throughput from the detector has been estimated to be about 3.5 TB/s for Pb-Pb collisions [13]. This leads the ALICE Computing Model to focus on reducing the data as much as possible as early as possible, in order to minimize the cost and requirements of the data processing and storage. This will be achieved by reconstructing the data on the fly in parallel with the data taking, in several steps. The final products of this data reduction are the Analysis Object Data (AOD) files, which contain the kinematics of the reconstructed tracks and the information of the particle identification (PID) detectors (in the case of simulated data, these files also contain the true identity of the tracks and the decay trees). These files will be written to the disk and serve as input for the Online-Offline (O^2) analysis software framework [14]. [13, 15]

3.1.1 The O^2 heavy flavour analysis framework

The analysis in this thesis is performed with the heavy flavour (HF) analysis framework in O^2, with the help of a separate package called `Run3Analysisvalidation` [16]. The latter, originally designed to compare (validate) the results of the run 3 software with the results of the run 2 software (`AliPhysics`), is in our case used to run the O^2 software package with the desired configuration. Contrary to its name, the package can be used to run (and in theory also validate) simulated run 5 data.

The O^2 analysis software is designed in a modular way, with data objects such as tracks and collisions represented by flat tables to maximize the processing performance. Rows in such a table correspond to a single instance of an object, with the columns corresponding

to properties of said object (e.g. transverse momentum of a track, vertex of a collision).[1] One is able to add an index column to a given table, which allows the user to store the index of a given object in another table, instead of the whole object. This is particularly useful when one wants to keep track of the specific daughters of a track. An analysis task can "subscribe" to and produce any given number of tables. An entire analysis, such as the one performed in this thesis, usually consists of multiple analysis tasks where the output table of one task is (one of) the input tables of the next.

The HF analysis framework consists of a series of analysis tasks and derived tables; an extensive overview of its workflow can be seen in Figure 3.1. The reconstruction of HF candidates (potential HF particles) requires several computationally or time intensive steps, including but not limited to multiple loops over the AOD tracks and secondary vertex reconstruction. To limit the time and computational resources needed, the HF reconstruction relies on a two-step skimming phase. This skimming task first performs computationally light calculations of variables, such as an approximate distance of closest approach (DCA), applying very loose selection criteria based on these calculations. It is worth noting that there is no significant efficiency loss expected at this stage, because the selection criteria are indeed very loose [13]. In the next step, it reconstructs the secondary vertex using the Newton-Raphson method [17], before propagating the tracks of the skims to the secondary vertex using a Kalman algorithm [18]. A first selection is applied on properties such as the candidate p_{T} and the cosine of pointing angle (CPA, defined as the cosine of the angle between the momentum of the reconstructed candidate and the line connecting the primary and secondary vertex). The final output of this skimming task is a table consisting of pairs and/or triplets of charged tracks that have survived the cuts, also called *skims*. [13]

These skims are then passed on to the candidate creator task, which rebuilds the secondary vertex. Additional properties of the HF candidates that are needed for detailed candidate selections are calculated and stored in the *candidate table*, together with the kinematics needed for the candidate selections. Note that these additional properties are usually computationally intensive, so they are not calculated in the skimming stage because they would then also be calculated for candidates that would immediately be rejected afterwards, wasting computational resources. In the case of simulated data, the candidate creator task also performs the so-called Monte Carlo (MC) matching. This matches candidates with their generated particles if it is indeed a "true" candidate, and stores the information in the candidate table. This allows for analysis of the signal/background and efficiency at a later stage.

The final two steps are quite straightforward. The candidate selector task applies selection cuts based on the properties in the candidate table, storing the information in a

[1] Note that not all columns are stored as "raw" data. Take the p_{T} for instance: the momentum of a track is stored in *static* columns as p_x, p_y, p_z, while the p_{T} is stored in a *dynamic* column as $\sqrt{p_x^2 + p_y^2}$. When called, the p_{T} is calculated on the fly with the static columns as arguments.

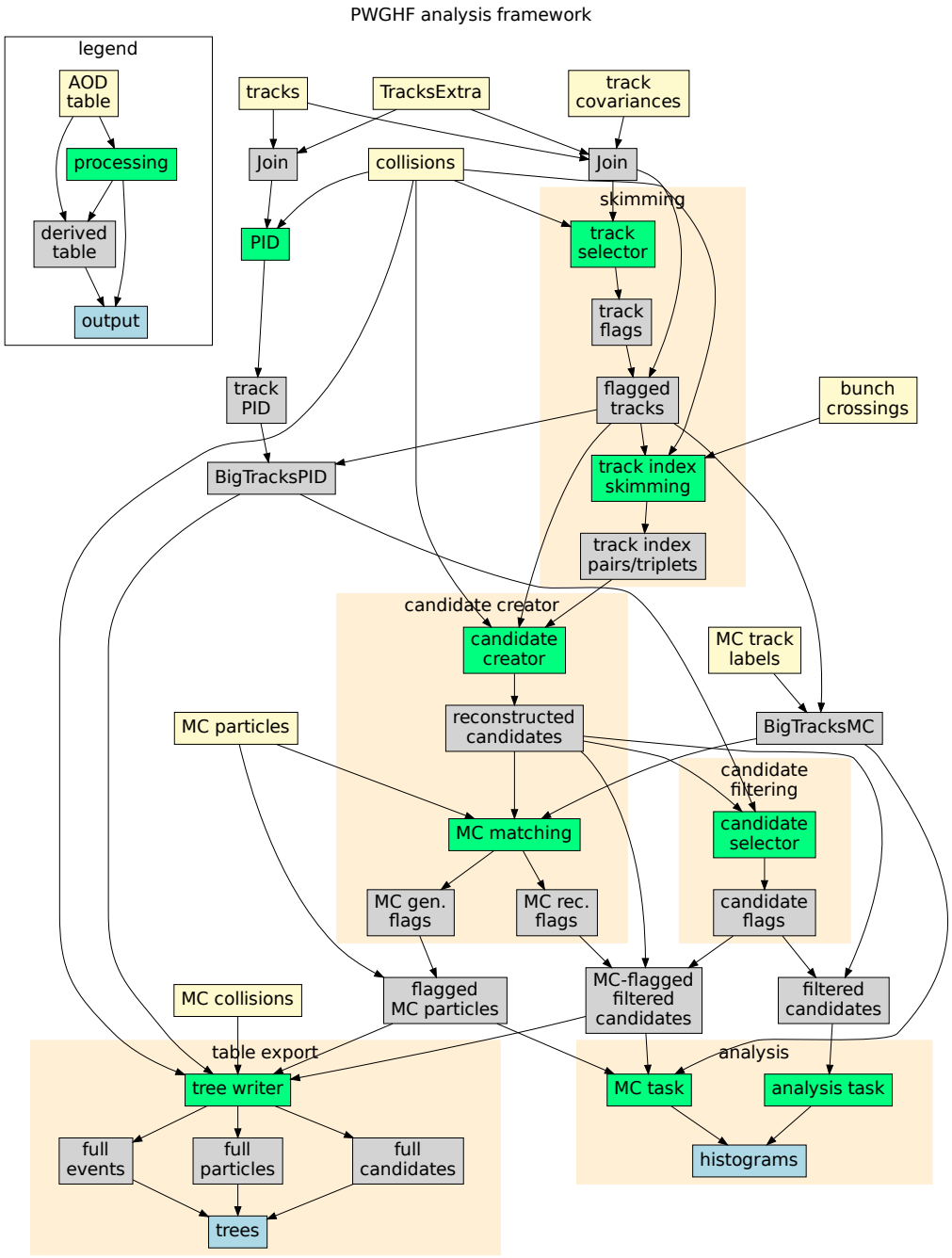

Figure 3.1: Complete overview of the HF analysis framework in O^2 for a non-cascading decay. Figure taken from [13].

small separate table. This separate table can easily be joined (appended) to the candidate table, since they contain identical rows. The final analysis task mostly creates histograms with properties of the selected candidates. In the case of simulated data it also creates histograms of the same properties separated by signal and background.

3.1.2 The X(3872) analysis framework

All the steps described in the previous section apply to heavy flavour particles that decay to particles we directly measure in our detector, such as $J/\psi \to e^+e^-$. To perform an analysis with a cascading decay such as X(3872) $\to J/\psi\ \pi^+\pi^-$ with $J/\psi \to e^+e^-$, we can make use of the modular structure of O^2 by building the X(3872) $\to J/\psi\ \pi^+\pi^-$ analysis on top of the $J/\psi \to e^+e^-$ one, see Figure 3.2.

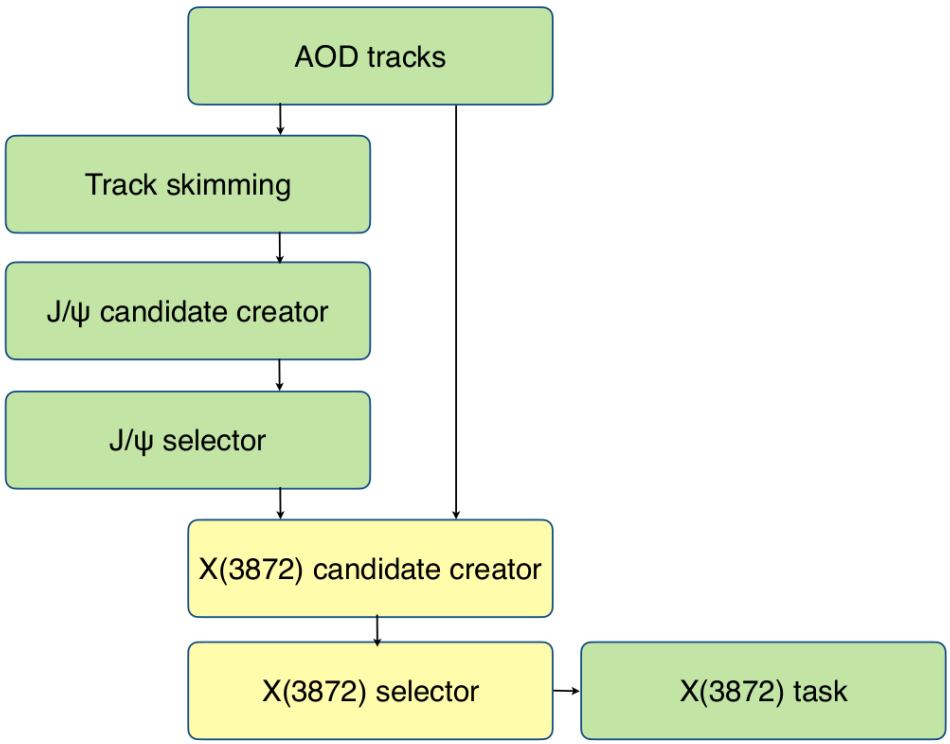

Figure 3.2: Compact workflow of the X(3872) analysis with the O^2 HF analysis framework.

We do this by making a separate candidate creator specifically for the X(3872), that subscribes to the AOD table and the combined (joined) table of the $J/\psi \to e^+e^-$ candidate and selector table. This X(3872) candidate creator skips the skimming stage entirely[2] by rebuilding the J/ψ decay vertex before immediately reconstructing the X(3872) decay

[2]Note that the skimming stage is still applied to $J/\psi \to e^+e^-$

vertex by combining the J/ψ with two oppositely charged tracks. As described in the previous section, the X(3872) candidate creator determines the relevant properties, fills the candidate table, and performs the MC matching. The X(3872) candidate selector then applies selection cuts in an analogous way, and the X(3872) analysis task creates the desired histograms.

3.2 MC simulations and detector layout

For our analysis we use AOD files containing data of pp collisions at $\sqrt{s} = 14$ TeV, generated by Monte Carlo (MC) simulations. This data is generated with the help of `PYTHIA` 8.2, a program designed for the generation of events in high-energy collisions [19]. Two different data sets (productions) are used: an enhanced production where the X(3872) is manually added, which from now on will be referred to as "Onia", and a minimum bias (MB) production. In the Onia enhanced production the X(3872) is forced to decay into $J/\psi\ \pi^+\pi^-$, where the J/ψ can only decay into e^+e^- or $\mu^+\mu^-$. This production is used for signal extraction, while the MB production is used to determine the background.

These simulations include a parametrization the detector performance, which is dependent on the layout of the relevant detectors. This allows for comparison of different detector layouts by analyzing different productions. For this analysis we use the detector layout v_1 (previously referred to as scenario 3) for the tracking system, with a TOF and ring-imaging Cherenkov (RICH) detector for particle identification. The specifications of the tracking system and TOF are derived from the ALICE 3 specifications document [20], with the tracking system parameters presented in Figures 3.3 and 3.4. The complete TOF detector consists of an outer, inner, and forward TOF located at $r = 1.00$ or 1.25 meter, $r = 0.2$ meter, and $z = 3.0$ meter respectively. The RICH detector, which measures the radiation emitted when a particle traverses a refractive medium, is implemented with a radius of 1 meter, length of 2 meter (in both z-directions, so 4 meter total), radiator length of 2 cm, refractive index of 1.03, efficiency of 0.4, and uncertainty of 0.007.

3.3 Selection strategy

When reconstructing particles from a certain decay mode, one may expect that by pure coincidence there are combinations of potential daughters that have a similar invariant mass. It could for instance be that there are two electrons originating from different processes that have an invariant mass corresponding to the J/ψ. These "false positives" are referred to as the combinatorial background, and the objective is to find ways to reduce this background while not reducing the "true positives". In general, selection strategies are devised to do exactly this by imposing criteria such that background candidates will not pass the selections, but most (ideally all) signal candidates will.

layer	radius (m)	length (m)	material (% X/X0)	resolution (um)
0	0.0050	2 x 0.15	0.1	2.5 (1.0?)
1	0.0120	2 x 0.15	0.1	2.5 (1.0?)
2	0.0250	2 x 0.15	0.1	2.5 (1.0?)
3	0.0375	2 x 0.62	0.1	2.5 (1.0?)
4	0.0700	2 x 0.62	1.0	10
5	0.1200	2 x 0.62	1.0	10
6	0.2000	2 x 0.62	1.0	10
7	0.3000	2 x 0.62	1.0	10
8	0.4500	2 x 1.32	1.0	10
9	0.6000	2 x 1.32	1.0	10
10	0.8000	2 x 1.32	1.0	10
11	1.0000	2 x 1.32	1.0	10

Figure 3.3: Table with the specifications of the barrel layers based on the technology described in Section 2.4. Table taken from [20].

disk	z (m)	R_i (m)	R_o (m)	material (% X/X0)	resolution (um)
0	0.16	0.005	0.03	1.0	10
1	0.20	0.005	0.03	1.0	10
2	0.24	0.005	0.03	1.0	10
3	0.77	0.005	0.35	1.0	10
4	1.00	0.005	0.35	1.0	10
5	1.22	0.005	0.35	1.0	10
6	1.50	0.005	1.00	1.0	10
7	1.80	0.005	1.00	1.0	10
8	2.20	0.005	1.00	1.0	10
9	2.79	0.005	1.00	1.0	10

Figure 3.4: Table with the specifications of the endcap layers based on the technology described in Section 2.4. Table taken from [20].

3.3.1 $J/\psi \rightarrow e^+e^-$ selection criteria

The strategy of selecting pairs of oppositely charged tracks as electrons originating from a J/ψ relies mostly on particle identification with the TOF and RICH, combined with selection criteria on the p_{T} and DCA of the two electrons. The criteria on the p_{T} and DCA, together with the invariant mass window considered can be seen in Table 3.1. For electrons with $0.5 < p_{\mathrm{T}} < 1.0$ GeV/c both the TOF and the RICH are required to identify the track as an electron with 3σ, while for $p_{\mathrm{T}} > 1.0$ GeV/c only the RICH is required (again with 3σ). Here $n\sigma$ denotes the number of standard deviations from the theoretical curve, within which a particle is "accepted". For $0.15 < p_{\mathrm{T}} < 0.5$ GeV/c we only require

the TOF, but this is not relevant for our analysis since we only consider electrons with $p_T > 0.5$ GeV/c, with an even harsher preselection of $p_T > 0.7$ GeV/c

Δm (GeV/c^2)	DCA_{xy} (cm)	DCA_z (cm)	min. p_T e (GeV/c)
0.5	0.2	0.4	0.5

Table 3.1: Selection criteria for the $J/\psi \to e^+e^-$ decay.

3.3.2 X(3872) $\to J/\psi\ \pi^+\pi^-$ selection criteria

The X(3872) selection strategy differs significantly from the J/ψ one, in that it relies more on the kinematics of the decay rather than directly on the particle identification. The complete set of kinematic and topological selection criteria can be found in Table 3.2. Two oppositely charged tracks are identified as pions by the TOF with 3σ, with a minimum p_T of 0.15 GeV. Although there is no explicit maximum p_T for the pions we require the p_T to be between 0.15 and 10 GeV for the TOF, thus placing an implicit cut on the maximum p_T. This should not have significant consequences however, since the pions are expected to be very soft.

p_T range (GeV/c)	Δm (GeV/c^2)	CPA	d0 (cm)		min. p_T (GeV/c)	
			J/ψ	π	J/ψ	π
$0 < p_T < 0.5$	0.5	0.80	0.001	0.001	0.0	0.15
$0.5 < p_T < 1$	0.5	0.80	0.001	0.001	0.0	0.15
$1 < p_T < 2$	0.5	0.80	0.001	0.001	0.2	0.15
$2 < p_T < 3$	0.5	0.80	0.001	0.001	0.9	0.15
$3 < p_T < 4$	0.5	0.80	0.001	0.001	1.5	0.15
$4 < p_T < 5$	0.5	0.80	0.001	0.001	2.3	0.15
$5 < p_T < 7$	0.5	0.90	0.001	0.001	3.0	0.15
$7 < p_T < 10$	0.5	0.90	0.001	0.001	4.2	0.15
$10 < p_T < 15$	0.5	0.90	0.001	0.001	6.2	0.15

Table 3.2: Selection criteria for the X(3872) $\to J/\psi\ \pi^+\pi^-$ decay.

As discussed in Section 2.4.1 the J/ψ inherits most of the p_T from the X(3872), so we require the minimum p_T of the J/ψ candidate to scale with the p_T of the X(3872),

albeit conservatively. This p_{T} dependence can explicitly be viewed in Figure 3.5. We also impose a maximum of 0.001 cm on the impact parameter of the prongs with the decay vertex of the X(3872), denoted by d0 to prevent ambiguity with the term interaction point (IP). The last notable selection is on the CPA, which gets more stringent with higher p_{T}. This is because the CPA is a topological variable on the angle between the decay line and reconstructed momentum of the X(3872). The decay line is the line between the primary and secondary vertex of the X(3872), which of course is longer in the case of higher momentum. In theory the CPA is exactly 1, but experimental uncertainties like the vertex resolution may cause deviations. The direction of a longer decay line is less sensitive to deviations from uncertainties of vertices, leading to a better defined CPA.

For both the X(3872) and J/ψ we require the rapidity $|y| < 1.44$, as well as the electrons. The pions are not limited explicitly by selection criteria, but by the acceptance of our simulated detector: $|\eta| < 4$.

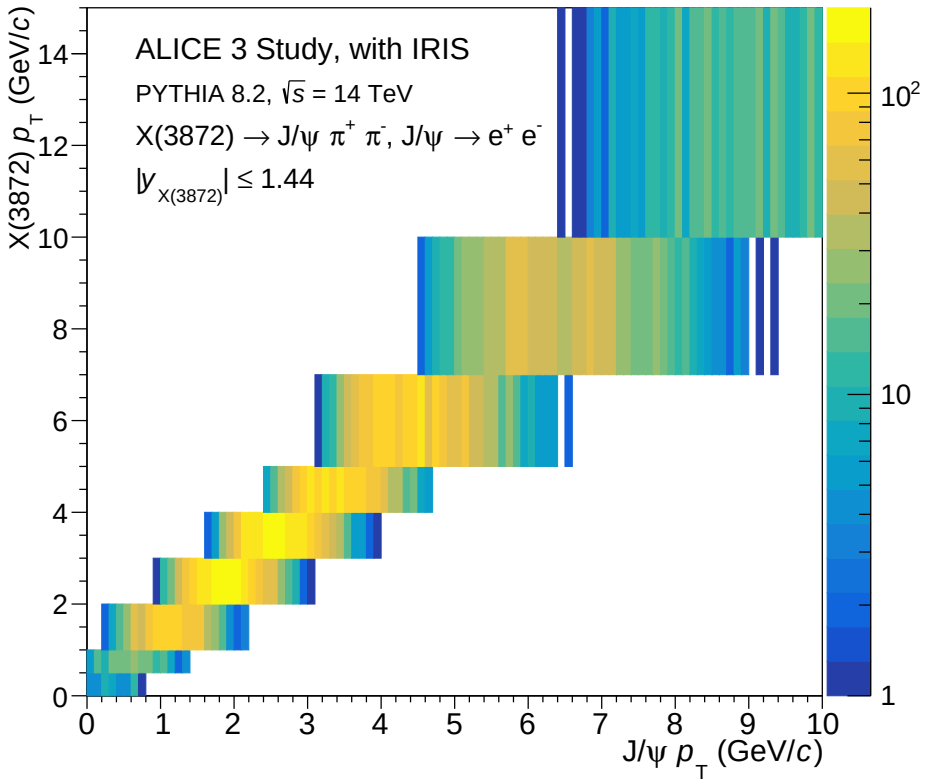

Figure 3.5: Transverse momentum of reconstructed X(3872) candidates versus the transverse momentum of its hypothetical daughter J/ψ. Note that there is no hard cutoff at the left edge of the J/ψ p_{T}, indicating that the minimum p_{T} cut on the J/ψ is conservative indeed.

To illustrate how selection criteria could be useful, we present some normalized distributions of signal and background candidates in Figure 3.6. The figures on the left represent distributions with $2 < p_{\mathrm{T}} < 4$ GeV/c, the figures on the right represent the same variable for $7 < p_{\mathrm{T}} < 10$ GeV/c. From top to bottom, the variables are the p_{T} of the J/ψ daughter, the p_{T} of the (positive) pion daughter, and the χ^2_{PCA} of the X(3872) decay vertex. The latter variable denotes the quality of the fit of the point of closest approach (PCA). In other words, it represents how well the algorithm was able to find a point where the distance to the J/ψ and pion tracks is minimized - this point corresponds to the X(3872) decay vertex. Note that we do not impose a selection criterion on this variable here.

Considering the signal and background distributions of the p_{T} of the J/ψ (Figures 3.6a and 3.6b), we can see that the distributions are quite similar. In Figure 3.6b the background distribution seems to have a small tail to the left, which is cut off by the minimum p_{T} selection.

The distributions of the p_{T} of the pion with lower p_{T} (Figure 3.6c) are also quite similar, while it seems that for higher p_{T} (Figure 3.6d) there is a disparity between signal and background. One may intuitively want to place a selection of $p_{\mathrm{T}} < 0.5$ GeV/c right after the peak of the background distribution, removing relatively more background than signal. However, removing such a significant amount of signal is generally undesirable, especially in the case of rare particles/decay modes such as the X(3872). This indicates that imposing selection criteria can require quite a nuanced approach.

Although we do not impose a selection criterion on the χ^2_{PCA}, we have included Figures 3.6e and 3.6f to show how these selections may reduce the background while leaving the signal distribution intact, but also to show how dependent on transverse momentum these selections can be. In Figure 3.6e it is clear that the background distribution has a much longer tail than the signal distribution, which does not seem to have much of a tail at all. This implies that a selection on this variable could relatively easily reduce the background, while keeping the signal distribution intact. However, at higher p_{T} (3.6f) it seems that the same selection would be much less effective. From the figure it is unclear whether this is due to an increased similarity between signal and background, or because the higher p_{T} allows for a better defined PCA. In any case, one should investigate this before imposing selection criteria on this variable.

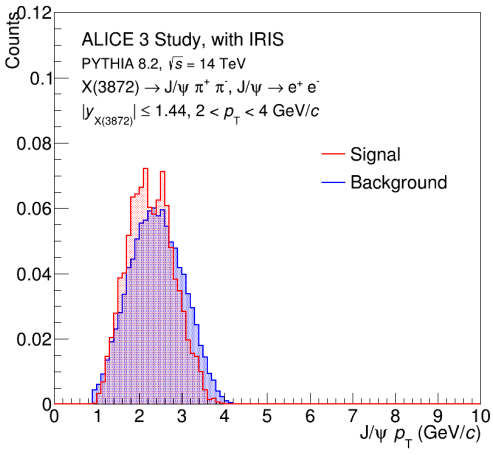

(a)

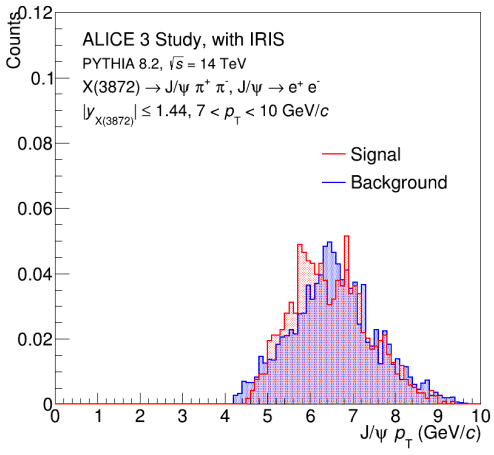

(b)

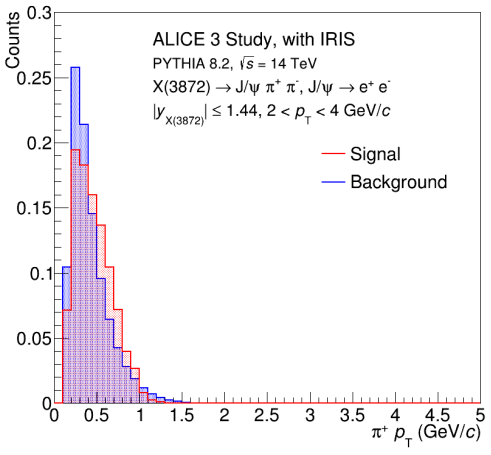

(c)

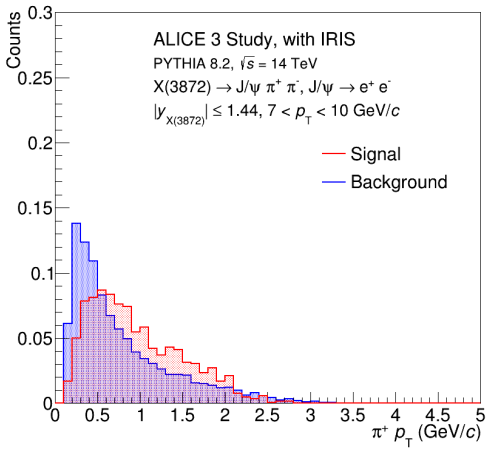

(d)

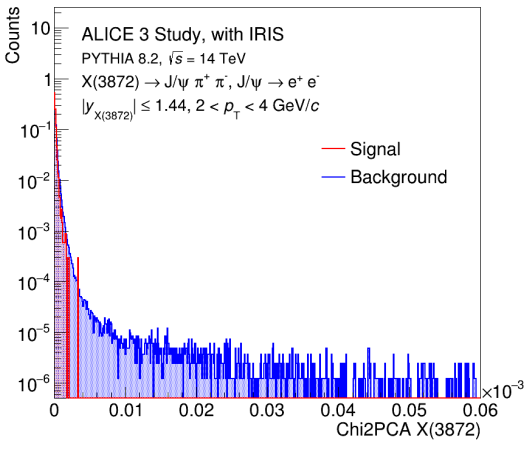

(e)

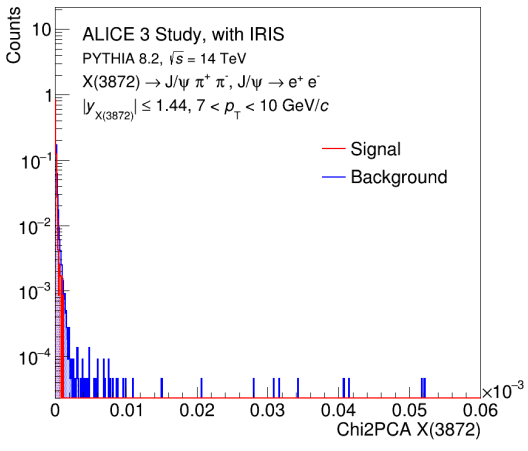

(f)

Figure 3.6

Chapter 4

Results

In this chapter we will present the results of the analysis, with the most crucial result being the significance of this measurement on the order of 10^{-1}. The significance in particle physics is defined as $S/\sqrt{S+B}$, where S and B stand for signal and background, respectively. Both the signal and background distributions are estimated via simulations, using a preliminary description of the detector setup which also includes inefficiencies that result into a lower signal yield than what nature produces. The sizes of the distributions are counted in a specified invariant mass region, usually $\pm 3\sigma$ from the mean of the invariant mass peak, where σ in this case denotes the standard deviation of the Gaussian distribution fitted to the mass peak. This region contains approximately 99.7% of the signal, and this is the convention used in this thesis. The significance is usually calculated as a function of transverse momentum.

4.1 Invariant mass

In Figure 4.1 we present the invariant mass of $J/\psi\ \pi^+\pi^-$ systems selected according to the criteria discussed in Section 3.3.2. The background consists of reconstructed candidates flagged as background extracted from the MB production. Since the X(3872) is not generated with the default settings (remember that it is manually added to the configuration of the signal production), all candidates are flagged as background. The signal distribution, plotted on top of the background, consists of reconstructed candidates flagged as signal candidates, extracted from the signal production. This means only the reconstructed candidates that are matched to a generated X(3872) are counted in the signal distribution. Although indicative of the width of the mass peak, the size of the mass peak is not physical since it is extracted from an enhanced production. The plots nonetheless illustrate that the mass peak is more pronounced at high transverse momentum.

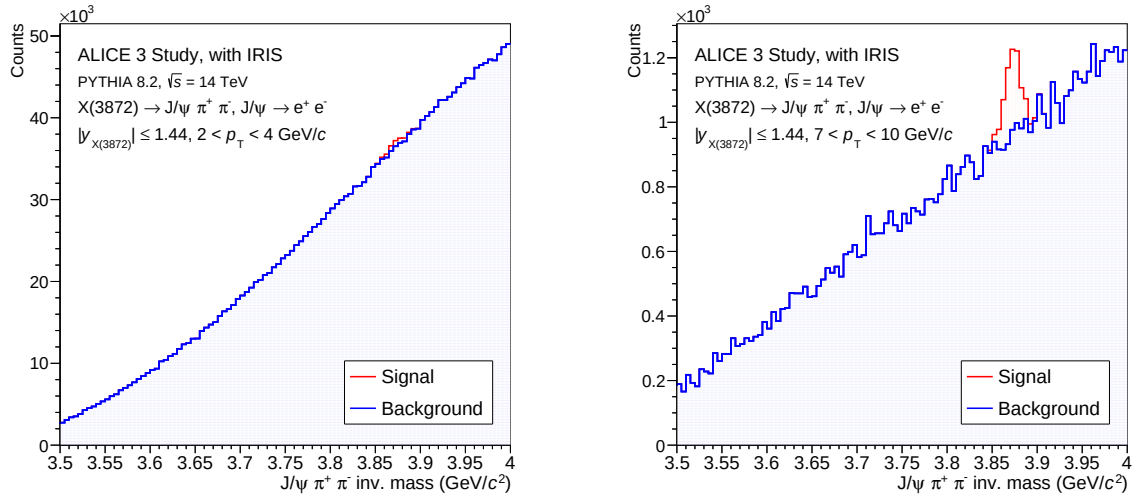

(a) Candidate p_{T} between 2 and 4 GeV/c. (b) Candidate p_{T} between 7 and 10 GeV/c.

Figure 4.1: Invariant mass of the $J/\psi\ \pi^+\pi^-$ system for two different transverse momentum regions. Note that the signal distributions are extracted from an enhanced signal production, the sizes are therefore not physical.

4.2 Efficiency

When analyzing simulated data, one is able to match "true" reconstructed particles (signal candidates) with their generated counterparts. A "false" candidate will of course not have a generated counterpart, and therefore be considered a background candidate. The number of reconstructed signal candidates divided by the number of generated particles is defined to be the efficiency. This quantity is usually calculated and presented per units of transverse momentum and rapidity. The efficiency reflects the performance of the detector within a given acceptance - in other words, only generated particles within the acceptance are counted towards the total number. In our case the acceptance is given by $|y| < 1.44$ for electrons, J/ψ, X(3872), and $|\eta| < 4$ for pions.

In the case of reconstructed particles, the efficiency is of course dependent on the efficiency of its prongs. After all, one is only able to reconstruct candidates from tracks that are measured by the detector. Starting from the particles that are directly measured by the detector, we can see their efficiencies as a function of transverse momentum (a) and pseudorapidity (b) in Figure 4.2a. Following the order in which we reconstruct the X(3872) candidates, we start by looking at the electrons from which we build our J/ψ candidates. Noting that there is a minimum p_{T} selection on the electrons, we can see from Figure 4.2a that the efficiency for the electrons is close to one. From Figure 4.2b we can induce that although the efficiency decreases with increasing absolute pseudorapidity, it is still close to one - especially for higher p_{T} electrons. Hence the efficiency of the J/ψ is

mainly determined by the minimum p_{T} (pre)selection.

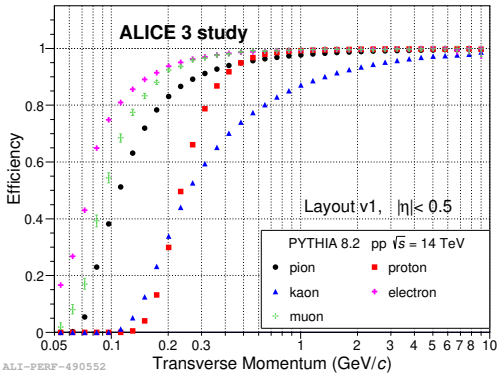

(a) Tracking efficiency of different charged particles as a function of p_{T}, with $|\eta| < 0.5$.

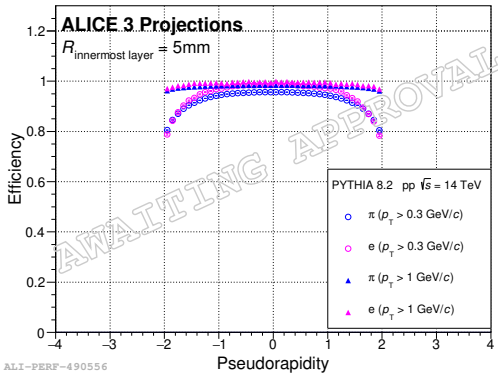

(b) Tracking efficiency of pions and electrons as a function of η, for $p_{\mathrm{T}} > 0.3$ GeV/c and $p_{\mathrm{T}} > 1.0$ GeV/c.

Figure 4.2: Tracking efficiency projections for ALICE 3. Although (b) is awaiting approval at the time of writing this thesis, it may still qualitatively indicate that the efficiency drops off with increasing absolute pseudorapidity. Figures taken from [21].

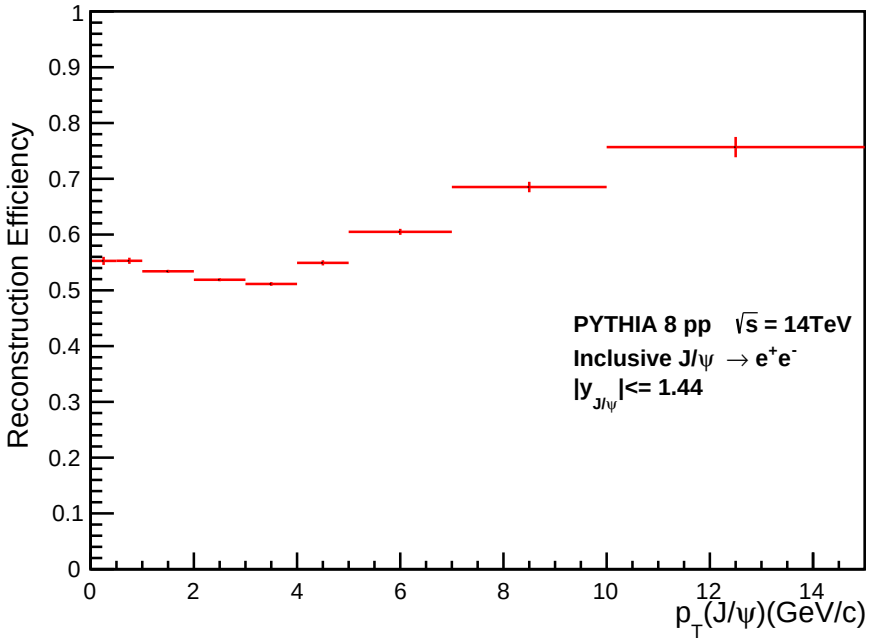

Figure 4.3: Efficiency of the J/ψ as a function of p_{T}. Figure taken from [22].

The efficiency of the J/ψ, including particle identification, is presented in Figure 4.3. We see that the efficiency is highest at high transverse momentum, with an efficiency around 75% for $10 < p_{\mathrm{T}} < 15$ GeV/c. There is room for improvement at low p_{T}, with the efficiency reaching its minimum of just over 50% at $3 < p_{\mathrm{T}} < 4$ GeV/c. Reiterating that the efficiency of the X(3872) is constrained by the efficiency of the J/ψ, it is important to increase the J/ψ efficiency at low p_{T} in order to improve the X(3872) efficiency at low p_{T} (for the p_{T} of the X(3872) as function of the J/ψ p_{T}, recall Figure 3.5).

Considering the efficiency of the X(3872) requires us to inspect the transverse momentum spectra of the pions, presented as a function of X(3872) p_{T} in Figure 4.4. It is crucial to observe that the momentum of the pions is expected to be very low, even for pions originating from high p_{T} X(3872). Note especially that the vast majority of pions has $p_{\mathrm{T}} < 1$ GeV/c, with most even going below 0.5 GeV/c. Referring again to Figure 4.2a, the efficiency of pions ranges from 70% to 95% for p_{T} between 0.15 and 1.0 GeV/c. Also taking into account the decrease of efficiency with increasing absolute pseudorapidity (Figure 4.2b), we may expect the efficiency to be limited by this as well (remember that the pions are allowed to have $|\eta| < 4$). On the other hand, it should be noted that units of rapidity do not correspond to equal angle of the detector - in other words, $3 < \eta < 4$ covers a smaller "slice" of the detector than $0 < \eta < 1$, and therefore represents a smaller yield of particles. This could make the decrease of total efficiency in Figure 4.2b less dramatic than one might infer.

Finally, we present the efficiency of the X(3872) in Figure 4.5. We note that there is quite an extreme p_{T} dependence, most likely due to the fact that both the J/ψ and pion efficiency scale with p_{T}. Starting at a few percent at low p_{T}, the efficiency increases to roughly 22% at $10 < p_{\mathrm{T}} < 15$. Although efficiencies of rare and heavy hadrons are often quite low, we may expect room for improvement here. Multiplying the approximate efficiencies of the J/ψ and pions at low p_{T} gives us a ballpark estimate of $0.5 \times 0.7 \times 0.7 = 0.245$ (0.5 as a low estimate of the J/ψ efficiency, and 0.7 for each of the pions), or roughly 25%. This is still well above the efficiency for X(3872) with low p_{T}, as can be seen in Figure 4.5.

4.3 Significance

Calculating the significance of this measurements requires extracting the signal and the background distributions. This is usually done with the help of the invariant mass distributions. The significance is presented as a function of transverse momentum, hence the following procedures are repeated for each and every p_{T} bin.

4.3.1 Background estimation procedure

The background is estimated by fitting a polynomial to the background distribution extracted from the MB production. We exclude the 3σ signal region to make sure we do

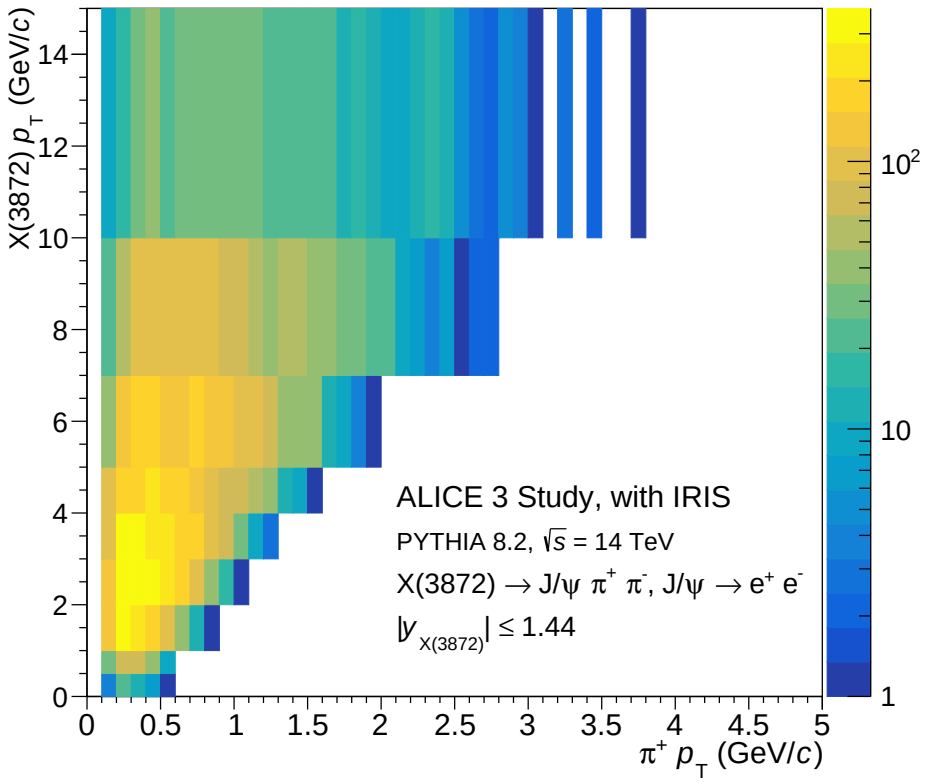

Figure 4.4: Transverse momentum of reconstructed X(3872) candidates versus the transverse momentum of its hypothetical positive pion daughter. Since both the positive and negative pions are from the same QCD process, their p_{T} spectra are very similar.

not incorporate any signal in the background fit.[1] We start by fitting a 2nd degree polynomial, increasing the degree until the reduced chi-squared (χ^2_{red}) is less than 3 or until the maximum polynomial degree is reached. This polynomial is then integrated over the signal region to determine the size of the background. We also divide by the number of events in our data to obtain the background per event, this allows us to later scale the significance with $\sqrt{N_{\mathrm{events}}}$, where N_{events} is the expected number of events for run 5.

4.3.2 Signal estimation procedure

Since the signal distribution is extracted from an enhanced production, we must scale it to extract the physical signal distribution - or rather the size of the signal. To this end,

[1] In the case of the X(3872) this is actually redundant, since `PYTHIA` does not generate X(3872) with the default settings used to produce the MB sample. For consistency with other analyses in the HF framework, we choose to apply the same background analysis.

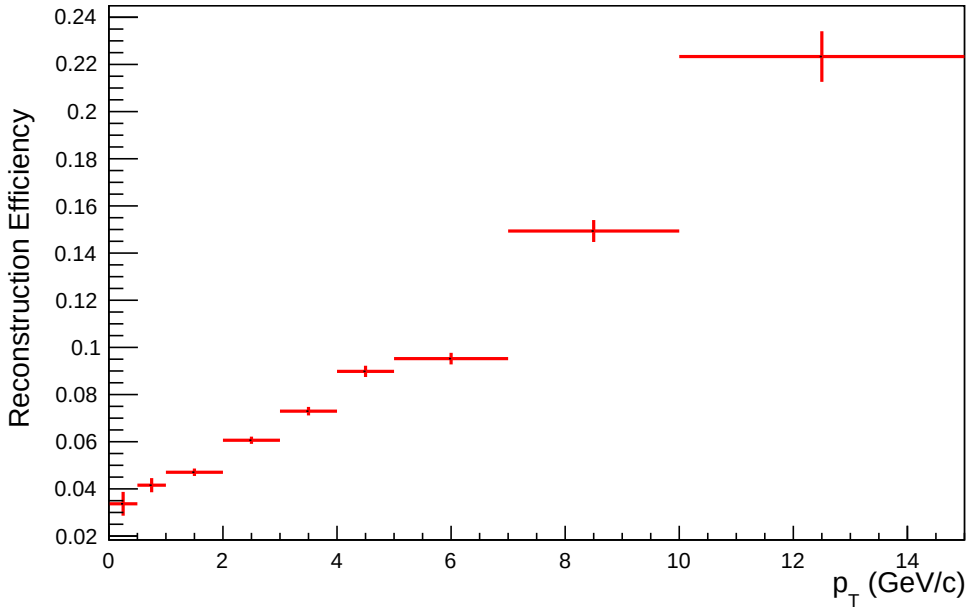

Figure 4.5: Efficiency of the X(3872) as a function of p_{T}. Note the different y-axis scale compared to Figure 4.3.

we calculate the signal per event for a given transverse momentum interval according to Equation 4.1.

$$S = \mathrm{BR}(\mathrm{X}(3872) \to J/\psi\, \pi^+\pi^-) \times \mathrm{BR}(J/\psi \to e^+e^-) \times \epsilon(p_{\mathrm{T}}) \times \sigma_{\mathrm{X}(3872)}(p_{\mathrm{T}}), \quad (4.1)$$

where $\epsilon(p_{\mathrm{T}})$ denotes the efficiency presented in Section 4.2, BR the branching ratios of the relevant decays, and $\sigma_{\mathrm{X}(3872)}(p_{\mathrm{T}})$ the production cross section of X(3872) as implemented in `PYTHIA`. Since the cross section of the X(3872) is unknown, we approximate it by multiplying the cross section of the $\psi(2S)$ as implemented in `PYTHIA` by the experimentally determined ratio of X(3872) to $\psi(2S)$, taking into account the difference in branching ratios. This is given in Equation 4.2.

$$\begin{aligned}\sigma_{\mathrm{X}(3872)} \approx \sigma^{\texttt{PYTHIA}}_{\psi(2S)} \times &\left(\frac{\sigma_{\mathrm{X}(3872)}\ \mathrm{BR}(\mathrm{X}(3872) \to J/\psi\, \pi^+\pi^-)}{\sigma_{\psi(2S)}\ \mathrm{BR}(\psi(2S)) \to J/\psi\, \pi^+\pi^-)}\right)_{\mathrm{exp}} \\ &\times \frac{\mathrm{BR}(\psi(2S)) \to J/\psi\, \pi^+\pi^-)}{\mathrm{BR}(\mathrm{X}(3872) \to J/\psi\, \pi^+\pi^-)},\end{aligned} \quad (4.2)$$

where the second term is approximated to be 0.1, extracted from [23]. The branching ratios in the third term are both extracted from [24]. This simplifies to $\sigma_{\mathrm{X}(3872)} \approx 0.8458\ \sigma^{\texttt{PYTHIA}}_{\psi(2S)}$, where the $\psi(2S)$ cross section is dependent on p_{T}.

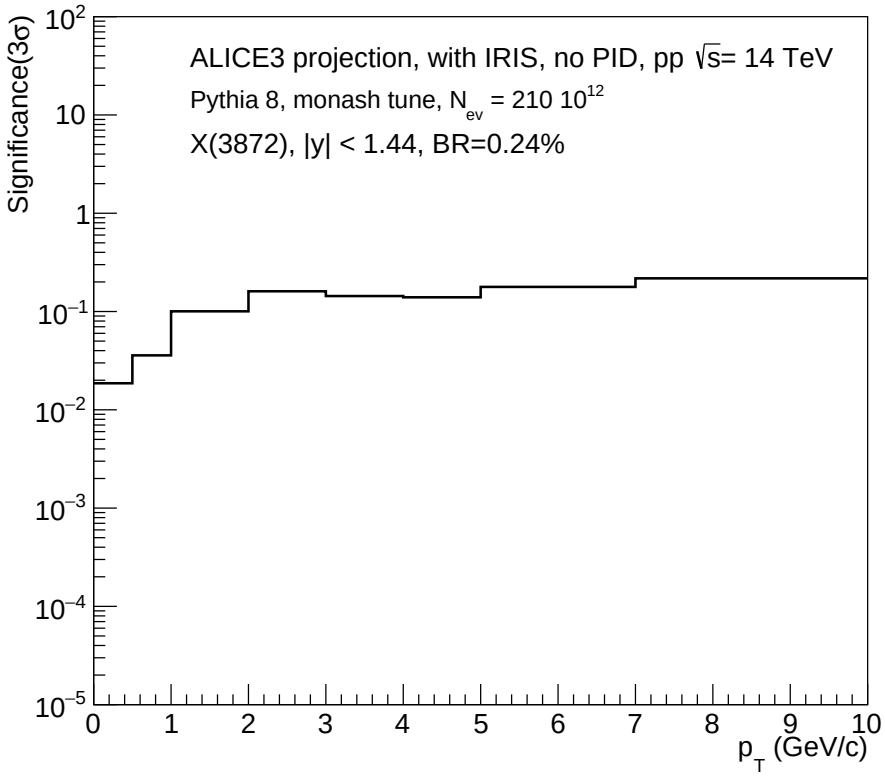

Figure 4.6: Significance of the measurement within the 3σ mass window, presented as a function of transverse momentum. The branching ratio reflects the total branching ratio of X(3872) $\rightarrow J/\psi\ \pi^+\pi^-$, with $J/\psi \rightarrow e^+e^-$

Now that we have both the signal and background per event, we may calculate the significance per event and multiply it by the number of events expected for run 5 to yield the total significance, presented in Figure 4.6. As can be seen, the significance is quite low across the whole transverse momentum spectrum, although it does increase with higher p_{T}. This is partially expected of course, since the X(3827) is difficult to reconstruct, adding on top of this the low branching ratios of the relevant decays. One should also note the lack of optimization in the selection strategy: most criteria were determined by looking at signal versus background distributions over a few iterations of analyses. A better optimized selection strategy should substantially increase the significance.

4.4 A different selection strategy

No extensive analysis was performed to determine the selection strategy presented in Section 3.2, which we will refer to from now on as the default strategy. To give an insight on the effect different strategies could have on the results and to provide a preliminary look into how such a strategy may differ from the default one, we present here the results of a different selection strategy. This strategy differs in only one aspect: the criterion on the CPA was removed for the entire transverse momentum region, instead of ranging from 0.8 to 0.9 in the default strategy. The efficiency and significance are presented in Figures 4.7 and 4.8 respectively.

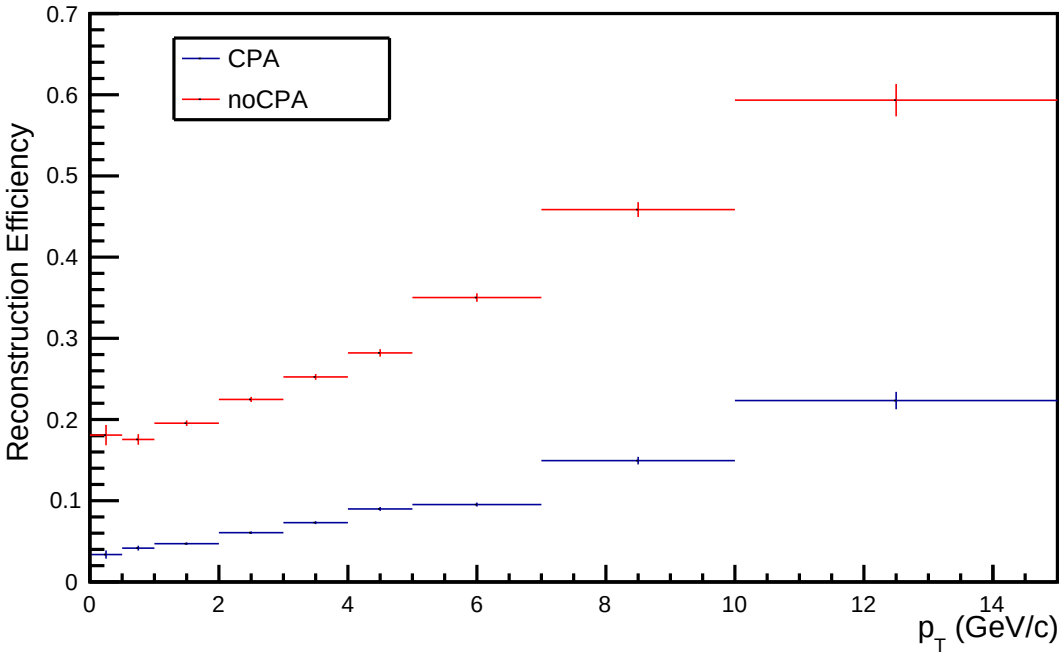

Figure 4.7: Efficiency of the X(3872) as a function of p_{T}. The efficiency with CPA selection is in blue, without in red.

As one can see, the efficiency drastically increases when removing the CPA selection. This could be due to the fact that, as discussed in Section 3.3.2, the CPA is much better defined for longer decay lines. Since the decay X(3872) $\rightarrow J/\psi\ \pi^+\pi^-$ is governed by the strong interaction, the lifetime and therefore decay line is expected to be rather short. This could mean that due to experimental uncertainties the CPA simply deviates too much from 1 to be an effective selection variable. The benefit of such a drastic increase in efficiency is large, although it is not synonymous with an increase in significance. The efficiency only positively affects the signal part of the significance (see Equation 4.1),

so it is completely possible that while the signal increases, the background increases even more leading to an overall decrease in significance. This is not the case with this selection strategy, as we can see in Figure 4.8 that the significance actually increases by approximately a factor of 2. This could be explained by the large increase in statistics resulting from loosening the CPA criterion, since the significance scales with $\sqrt{N_{\text{events}}}$.

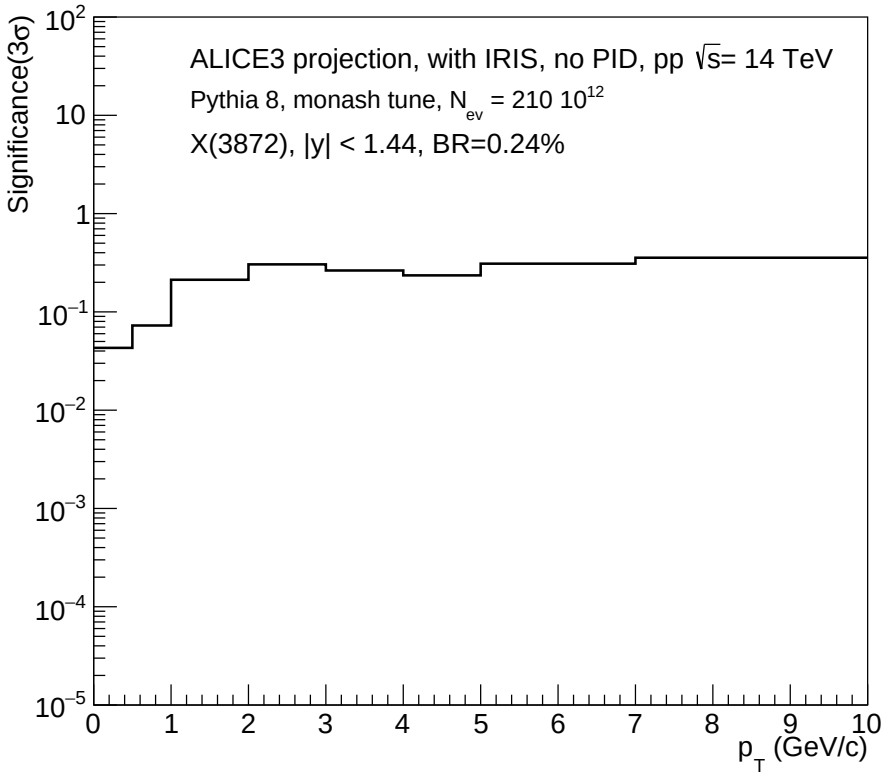

Figure 4.8: Significance without the CPA selection criterion.

Chapter 5

Conclusion

In this thesis we have performed simulation studies on the exotic X(3872) hadron via its decay to $J/\psi\ \pi^+\pi^-$ with $J/\psi \to e^+e^-$ in pp collisions at $\sqrt{s} = 14$ TeV for ALICE 3 with the O^2 software framework. Reconstructing this decay is challenging due to the short lifetime of the X(3872) and the low transverse momentum of the pion daughters. ALICE 3 will, on top of being able to process much higher luminosities, be able to measure tracks down to very low transverse momentum, making the X(3872) a very interesting and possibly feasible research avenue for run 5. We have implemented the X(3872) $\to J/\psi\ \pi^+\pi^-$ reconstruction on top of the already existing $J/\psi \to e^+e^-$ one, taking advantage of the modular structure of O^2. With the (preliminary) default selection strategy we find an efficiency ranging from approximately 0.03 to 0.22 for the transverse momentum range of 0 to 15 GeV/c. A significance on the order of 10^{-1} is reported, but for the transverse momentum region of 0 to 1 GeV/c the significance is substantially lower at $\sim 0.02 - 0.04$.

We have also implemented a different selection strategy by removing the CPA criterion. This strategy yielded an efficiency ranging from approximately 0.19 to 0.6 and roughly doubled the significance across the transverse momentum spectrum, possibly due to the increase in statistics as a consequence of removing the CPA criterion. This emphasizes that the default strategy is barely optimized, and that there is much room for improvement. This improvement may come in the form of sequentially fine-tuning the selection criteria by iterating, adding more selection variables that give a good separation of signal and background, using machine learning techniques to optimize the selection strategy, or any combination of these methods. One example of a selection variable that may be added to the strategy is a variable also used by CMS [25] denoted by $\Delta R = \sqrt{(\Delta\eta)^2 + (\Delta\phi)^2}$, where $\Delta\eta$ and $\Delta\phi$ are differences in pseudorapidity and azimuthal angle between the J/ψ and (one of) the pion candidates.

The background is extracted directly from the MC generated minimum bias production, without correcting for any possible discrepancy between the generated data and real data. One could work out the ratio between the background from real and gener-

ated data, possibly scaling for the collision energy, and multiplying the background from this analysis with this ratio. This would give a more realistic view of the combinatorial background. Although this procedure is not applicable to the signal extracted from the enhanced production, one could still improve the realisticness of the signal by estimating the production cross section of X(3872) in a more sophisticated way.

Production studies in heavy ion collisions have been proposed to constrain the nature of the X(3872) to a tetraquark or $D^0 - \bar{D}^{*0}$ molecule. Adding onto this that charm quarks are considered excellent probes for the QGP due to their early production, it would be interesting to scale the significance of this measurement from pp to Pb-Pb collisions to analyze the yield of the X(3872) in heavy ion collisions. Related to this, it would be interesting to perform this analysis on generated AA collisions for run 5, once these productions are available.

All things considered there is a lot of potential for the measurement of the X(3872) particle with ALICE 3, not just on the nature of this exotic hadron but also considering studies on the quark-gluon plasma.

Bibliography

[1] Wikipedia page on the Standard Model, July 2021.

[2] The Belle Collaboration, S.-K. Choi, and S. L. Olsen. Observation of a narrow charmonium-like state in exclusive B+ -> K+ pi+pi- J/psi decays. *Physical Review Letters*, 91(26):262001, December 2003. arXiv: hep-ex/0309032.

[3] Hui Zhang, Jinfeng Liao, Enke Wang, Qian Wang, and Hongxi Xing. Deciphering the nature of X(3872) in heavy ion collisions. *Physical Review Letters*, 126(1):012301, January 2021. arXiv: 2004.00024.

[4] Angelo Esposito, Elena G. Ferreiro, Alessandro Pilloni, Antonio D. Polosa, and Carlos A. Salgado. The nature of x(3872) from high-multiplicity pp collisions. *arXiv:2006.15044 [hep-ph, physics:nucl-th]*, June 2020. arXiv: 2006.15044.

[5] LHCb Collaboration et al. Multiplicity-dependent modification of χc1 (3872) and ψ (2s) production in pp collisions at $\sqrt{s} = 8$ tev. In *LHCb-CONF-2019-005*, 2019.

[6] Esma Mobs. The CERN accelerator complex - 2019. Complexe des accélérateurs du CERN - 2019. July 2019.

[7] Elena Botta. Particle identification performance at ALICE. *arXiv:1709.00288 [nucl-ex]*, September 2017. arXiv: 1709.00288.

[8] The ALICE Collaboration. Performance of the ALICE experiment at the CERN LHC. *International Journal of Modern Physics A*, 29(24):1430044, September 2014.

[9] B Abelev et al and The ALICE Collaboration. Upgrade of the ALICE Experiment: Letter Of Intent. *Journal of Physics G: Nuclear and Particle Physics*, 41(8):087001, August 2014.

[10] Z Citron, A Dainese, JF Grosse-Oetringhaus, JM Jowett, Y-J Lee, UA Wiedemann, M Winn, A Andronic, F Bellini, E Bruna, and others. Future physics opportunities for high-density QCD at the LHC with heavy-ion and proton beams. *arXiv preprint arXiv:1812.06772*, 2018.

[11] S. Voloshin and Y. Zhang. Flow Study in Relativistic Nuclear Collisions by Fourier Expansion of Azimuthal Particle Distributions. *Zeitschrift für Physik C Particles and Fields*, 70(4):665–671, May 1996. arXiv: hep-ph/9407282.

[12] Dagmar Adamová, G Aglieri Rinella, M Agnello, Z Ahammed, D Aleksandrov, A Alici, A Alkin, T Alt, I Altsybeev, D Andreou, and others. A next-generation LHC heavy-ion experiment. *arXiv preprint arXiv:1902.01211*, 2019.

[13] Vit Kuçera. Analysis of heavy-flavour particles in ALICE with the O2 analysis framework. In *Internal note in preparation, to be published*, 2021.

[14] AliceO2Group/AliceO2, June 2021. original-date: 2014-10-07T16:00:34Z.

[15] P Buncic, M Krzewicki, and P Vande Vyvre. Technical Design Report for the Upgrade of the Online-Offline Computing System. Technical report, April 2015.

[16] AliceO2Group/Run3Analysisvalidation, June 2021. original-date: 2020-02-02T20:56:40Z.

[17] Tetsuro Yamamoto. Historical developments in convergence analysis for Newton's and Newton-like methods. *Journal of Computational and Applied Mathematics*, 124(1):1–23, December 2000.

[18] Rudolph Emil Kalman. A new approach to linear filtering and prediction problems. *Journal of Basic Engineering*, 82(1), 1960.

[19] Torbjörn Sjöstrand, Stefan Ask, Jesper R Christiansen, Richard Corke, Nishita Desai, Philip Ilten, Stephen Mrenna, Stefan Prestel, Christine O Rasmussen, and Peter Z Skands. An introduction to PYTHIA 8.2. *Computer physics communications*, 191:159–177, 2015. Publisher: Elsevier.

[20] ALICE Collaboration. ALICE 3 specifications. In *Authoritative source of specifications for ALICE 3 simulations and projections*, 2021.

[21] Marianna Mazzilli. Tracking and vertexing performance with ALICE3, June 2021.

[22] Biao Zhang. Status and prospects for J/psi detection with ALICE 3, June 2021.

[23] Morad Aaboud, G Aad, B Abbott, J Abdallah, B Abeloos, R Aben, OS AbouZeid, NL Abraham, H Abramowicz, H Abreu, et al. Measurements of ψ(2S) and X(3872) $\rightarrow$ J/ψ π+ π- production in pp collisions at $\sqrt{s}$= 8 TeV with the ATLAS detector. *Journal of High Energy Physics*, 2017(1):1–43, 2017.

[24] Particle Data Group, PA Zyla, RM Barnett, J Beringer, O Dahl, DA Dwyer, DE Groom, C-J Lin, KS Lugovsky, E Pianori, et al. Review of particle physics. *Progress of Theoretical and Experimental Physics*, 2020(8):083C01, 2020.

[25] S. Chatrchyan, V. Khachatryan, A. M. Sirunyan, A. Tumasyan, W. Adam, E. Aguilo, T. Bergauer, M. Dragicevic, J. Erö, and et al. Measurement of the X(3872) production cross section via decays to J/ψ $\pi^+\pi^-$ in pp collisions at $\sqrt{s} = 7$ TeV. *Journal of High Energy Physics*, 2013(4), April 2013. Publisher: Springer Science and Business Media LLC.